

Dislocations in SrTiO₃: Easy To Reduce but Not so Fast for Oxygen Transport

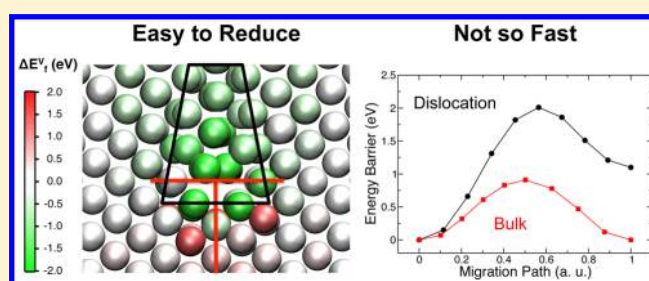
Dario Marrocchelli,[†] Lixin Sun,[†] and Bilge Yildiz^{*,†,‡}

[†]Laboratory for Electrochemical Interfaces, Department of Nuclear Science and Engineering, Massachusetts Institute of Technology, 77 Massachusetts Avenue, Cambridge, Massachusetts 02139, United States

[‡]Department of Materials Science and Engineering, Massachusetts Institute of Technology, 77 Massachusetts Avenue, Cambridge, Massachusetts 02139, United States

S Supporting Information

ABSTRACT: The effect of dislocations on the chemical, electrical and transport properties in oxide materials is important for electrochemical devices, such as fuel cells and resistive switches, but these effects have remained largely unexplored at the atomic level. In this work, by using large-scale atomistic simulations, we uncover how a $\langle 100 \rangle \{011\}$ edge dislocation in SrTiO₃, a prototypical perovskite oxide, impacts the local defect chemistry and oxide ion transport. We find that, in the dilute limit, oxygen vacancy formation energy in SrTiO₃ is lower at sites close to the dislocation core, by as much as 2 eV compared to that in the bulk. We show that the formation of a space-charge zone based on the redistribution of charged oxygen vacancies can be captured quantitatively at atomistic level by mapping the vacancy formation energies around the dislocation. Oxide-ion diffusion was studied for a low vacancy concentration regime (ppm level) and a high vacancy concentration regime (up to 2.5%). In both cases, no evidence of pipe-diffusion, i.e., significantly enhanced mobility of oxide ions, was found as determined from the calculated migration barriers, contrary to the case in metals. However, in the low vacancy concentration regime, the vacancy accumulation at the dislocation core gives rise to a higher diffusion coefficient, even though the oxide-ion mobility itself is lower than that in the bulk. Our findings have important implications for applications of perovskite oxides for information and energy technologies. The observed lower oxygen vacancy formation energy at the dislocation core provides a quantitative and direct explanation for the electronic conductivity of dislocations in SrTiO₃ and related oxides studied for red-ox based resistive switching. Reducibility and electronic transport at dislocations can also be quantitatively engineered into active materials for fuel cells, catalysis, and electronics.



1. INTRODUCTION

Dislocations are ubiquitous one-dimensional defects found in crystalline materials, including bulk,^{1,2} thin film,^{3–6} 2-D⁷ and nanoscale structures.^{7–9} As such, they can affect the properties of materials used in every technological application, including solid oxide fuel cells (SOFCs),¹⁰ catalysis,¹¹ resistive switching memories,¹² sensors,¹³ Li-ion batteries,¹⁴ photovoltaics,¹⁵ thermoelectrics¹⁶ and multiferroics.¹⁷ Metal oxides in the form of thin films, often used in strain engineering of relevant properties,⁵ show especially high concentrations of dislocations.^{3,6,18,19} However, despite their ample presence, the effect of dislocations on the electrical,^{20,21} chemical^{21–23} and transport^{20,22,24} properties in oxides is only scarcely explored at a local level. This is contrary to the maturity of knowledge on the compositional and diffusional properties of dislocations in metals.^{25–28} In this paper, by using atomistic simulations, we uncover how an edge dislocation in SrTiO₃ (a model and technologically relevant perovskite oxide) impacts the chemical and electrical properties of this material. We provide this work also as an illustrative example to coupled electro-chemo-

mechanical behavior in oxides,^{5,29} of interest to energy^{30,31} and information technologies.^{2,12,32,33}

The most prominent phenomenon tied explicitly to dislocations in SrTiO₃ is red-ox based resistive switching. Resistive switching is the ability of certain materials, such as SrTiO₃, to change their resistance state upon the application of an electric bias - a property that can enable high performance memories.¹² To date, several mechanisms have been suggested to explain the origins of this phenomenon.^{2,12,20,34–37} Perhaps the most convincing explanation comes from Szot and coauthors, who recently reviewed an impressive amount of literature and suggested that the electrical conductivity of this material under electrical bias is determined by the electrical properties of dislocations.² The hypothesis of the work in ref 2 is that “the extended dislocation acts as (pipe) diffusion path allowing preferential exchange of oxygen with the surroundings” under electric field, and thus the dislocations are preferentially reduced. Reduction of the SrTiO₃ along the dislocation, in turn,

Received: December 29, 2014

Published: March 9, 2015

increases the electronic conductivity of this material^{20,38–40} because of the lowering of the oxidation state of Ti ions, from 4+ to 3+, as also supported by theoretical studies.^{41–43} The higher conductivity of dislocations upon switching in SrTiO₃ has been demonstrated with Locally Conducting-Atomic Force Microscopy (LC-AFM) experiments,^{2,12,44} that show the formation of conducting filaments attributed to dislocations embedded in an insulating matrix. However, the key question is *what is really the mechanism for the preferential exchange of oxygen at dislocations: is it a thermodynamic factor (i.e., a lower oxygen vacancy formation energy) or is it a kinetic factor (i.e., preferential migration and exchange of oxygen along dislocations)?* Knowing the answers to this question quantitatively would help develop more accurate models for resistive switching kinetics.

A related question is the role of dislocations on the oxide ion conductivity of oxides. This is relevant because previous work has speculated that the resistive switching behavior of SrTiO₃ can be explained in terms of fast oxygen diffusion along a dislocation.^{12,34,44,45} Furthermore, other applications of oxides which rely on oxygen exchange and oxygen transport, such as solid oxide fuel cells, separation membranes and sensors, can benefit from structures that allow for fast oxide ion diffusion.⁴⁶ While dislocations are known to facilitate diffusion in metals by enhancing mobility, a phenomenon called *pipe-diffusion*,^{25–28} conduction of ions along dislocations in oxides is neither widely quantified nor agreed upon. Some researchers provide evidence that dislocations enhance^{19,47} and some suggest that they impede^{3,20,22} the mobility of oxide ions in SrTiO₃ and in other oxide materials. So, *do dislocations contribute to the resistive switching process through faster ionic conduction, or is it only electronic conduction that plays a role?* Recently, Metlenko et al. performed tracer diffusion and electrical conductivity measurements on SrTiO₃.²⁰ They found no evidence of fast diffusion along a dislocation array in a tilt grain boundary, though they could not exclude this possibility because of the limited sensitivity of the experimental approach. Their results were supplemented by a few static calculations of select migration paths and energy barriers, which showed no evidence of increased *mobility* of oxide ions along the dislocation. However, we note here that the diffusion coefficient depends both on the *mobility* and the *concentration* of oxygen defects, as shown by the following formula:⁴⁸

$$D(T) = [V_{\text{O}}^{\bullet\bullet}] \gamma a_0^2 \theta e^{-(E_m/k_B T)} = D_0(T) e^{-(E_m/k_B T)} \\ \text{with } [V_{\text{O}}^{\bullet\bullet}] \propto e^{-(E_f^V/k_B T)} \quad (1)$$

where D is the diffusion coefficient, $[V_{\text{O}}^{\bullet\bullet}]$ is the concentration of oxygen vacancies, γ is a constant, a_0 and θ are the jump distance and frequency, E_m is the oxide ion migration energy barrier, k_B is the Boltzmann constant and T is the temperature. $D_0(T)$ contains γ , a_0 , and θ , and the vacancy concentration $[V_{\text{O}}^{\bullet\bullet}]$. We note that the vacancy concentration is itself a function of temperature as it is proportional to $\exp(-E_f^V/k_B T)$, where E_f^V is the oxygen vacancy formation energy. Equation 1 therefore sets the stage for this paper, by showing that the oxide ion diffusion coefficient, D , depends both on mobility, via $\exp(-E_m/k_B T)$, and on the concentration of oxygen defects, $[V_{\text{O}}^{\bullet\bullet}]$, via $\exp(-E_f^V/k_B T)$. We recall here that pipe-diffusion implies a higher mobility, i.e., a lower migration energy barrier, E_m .²⁸ However, even if E_m is higher along the dislocation compared to that in bulk SrTiO₃, one could still obtain a higher diffusion coefficient, D , along a dislocation by increasing $[V_{\text{O}}^{\bullet\bullet}]$ due to a reduction in the formation energy of oxygen vacancies.

To deduce whether the diffusion coefficient of oxygen can be larger along dislocations in SrTiO₃, *both* the concentration and mobility terms will be explicitly assessed in the vicinity of the dislocation for the first time in this paper.

Driven by the above motivations, in this paper we use atomistic simulations to address two key questions: (1) *is it easier to create oxygen vacancies (i.e., is it easier to reduce SrTiO₃) near a dislocation, and by how much compared to the bulk SrTiO₃?*, and (2) *do dislocations enhance the oxide ion conductivity, or diffusion coefficient, in SrTiO₃?* As a result, we find that SrTiO₃ can be easily reduced at the dislocation core due to the under-coordination of oxide ions, with the oxygen vacancy formation energy being up to 2.0 eV lower than the bulk. No evidence of pipe-diffusion, i.e. enhanced oxide ion mobility, was found neither in a low vacancy concentration regime (ppm level) nor in a high vacancy concentration regime (up to 2.5%). However, for the case of low vacancy concentration, we found vacancy accumulation at the dislocation core, which in turn gives rise to a higher diffusion coefficient even though the oxide ion mobility is lower than that in the bulk.

2. METHODOLOGY

In this section, we briefly present the methodology employed in this work. For the sake of brevity, we report some technical details in the Supporting Information, as explained below.

2.1. Interionic Potential and Simulation Details. In this work we used the interionic potential developed by Thomas et al.⁴⁹ This potential was parametrized with reference to both experimental and *first-principles* data. It was shown to successfully reproduce the structural properties of SrTiO₃ and Sr₃Ti₂O₇,^{49,50} the bulk diffusion of oxide-ions⁵¹ and the stacking fault energy and {110}{110} dislocation structure of SrTiO₃,^{52,53} as well as other properties.^{54,54–56} This potential is a computationally fast rigid ion model, consisting of a Born-Mayer part to describe the short-range repulsion between ions and a Coulombic interaction. Partial charges are used which were derived from a Mulliken analysis of Density Functional Theory (DFT) data.⁴⁹ The parameters of this potential are also reported in Table S1 (Supporting Information).

The Thomas potential was originally parametrized for stoichiometric SrTiO₃ only. The study of reduced SrTiO_{3-δ} requires extra information on how to change the charge of Ti (and possibly also O and Sr) when this material is reduced. In previous work, Schie et al. have distributed the extra charge (resulting from the creation of oxygen vacancies) equally among all the Ti and O atoms.⁵¹ In this paper, we use a similar approach and modify the Ti and O charges (q_{Ti} and q_{O}), but with three times more charge assigned to each Ti cation than to each O anion, in accord with chemical intuition.^{42,43} The charge distribution is calculated by the following equations:

$$q_{\text{Ti}} = 2.36 - \frac{Q}{2n_{\text{Ti}}} \quad (2a)$$

$$q_{\text{O}} = -1.40 - \frac{Q}{2n_{\text{O}}} \quad (2b)$$

where Q is the total extra charge (e.g., 1.4 if one oxygen vacancy is introduced) and n_{Ti} and n_{O} are the number of Ti and O ions present in the system. We find that this yields a much better agreement with DFT calculations of the chemical expansion⁵⁷ and with the dependence of vacancy formation energy on lattice strain in SrTiO₃ (see Supporting Information Figures S1–S3). Finally, we note that the charges assigned according to eqs 2 are independent of the atom location.

We use the LAMMPS code to run Molecular Dynamics (MD) simulations at finite temperatures, as well as static relaxations at 0 K.⁵⁸ The simulated model with the dislocation will be reported in section 2.2. We simulate bulk SrTiO₃ with 20 × 20 × 20 unit cell system

($\sim 40\,000$ atoms) with no dislocations. We dub this system “dislocation-free bulk SrTiO_3 ” and use it as a reference throughout the paper. The dislocation-free bulk SrTiO_3 model is equilibrated in the NPT ensemble; longer runs (~ 5 ns) are then performed in the NVT ensemble. In all calculations, long-range Coulombic interactions are summed using the PPPM method,⁵⁹ as implemented in LAMMPS; the short-range part of the potential is calculated within a cutoff distance of 12 Å. Diffusion coefficients are extracted from the slope of the mean squared displacement (MSD) of the ionic species of interest, as done in previous work.^{22,60–64} Select migration barriers are calculated using the Nudged Elastic Band (NEB) method, as implemented in LAMMPS. We used between 5 and 10 images, depending on the migration pathway.

2.2. Dislocation Setup. The study of dislocations by means of atomistic simulations is complicated by their nonperiodic nature and large spatial extent. These two challenges are overcome in this study by simulating two noninteracting dislocations with opposite Burgers vectors, $\pm(100)$ on the $\{110\}$ slip plane, and by employing computationally efficient (though accurate) rigid-ion models, that allow us to simulate $\sim 160\,000$ atoms for sufficiently long time-scales (~ 30 ns). We note here that our approach allows us to focus on the role of a single dislocation, rather than a low-angle grain boundary with a periodic array of closely spaced dislocations, as studied in ref.²⁰ Furthermore, using LAMMPS, a massively parallelized software, allows us to model the dislocation system at suitably large spatial and temporal scales.²⁰

Two opposite $\langle 100 \rangle \{011\}$ edge dislocations are introduced in the simulation model as shown in Figure 1. The perovskite lattice structure is rotated to construct the x , y , and z -axes of the simulation model along the $\langle 0\bar{1}1 \rangle$, $\langle 100 \rangle$, and $\langle 011 \rangle$ crystallographic directions. These correspond to the dislocation line vector, Burgers vector, and slip plane normal, respectively. We introduce a cut in the middle of the box by removing two crystallographic planes (corresponding to a SrO and

a TiO_2 plane), as shown in Figure 1a. The cut is healed by structural optimization, and forms two edge dislocations at the upper and lower parts of the simulation box. The upper dislocation has a Burgers vector of $\langle 100 \rangle$ and the bottom $\langle \bar{1}00 \rangle$.

It is important to note that, when the crystal is cut as shown in Figure 1a, the surfaces exposed at the two ends of the cut (that later make the dislocation core) are polar. This is because the cut surfaces at the top and bottom are $\{011\}$ planes, which consist of alternating $(\text{SrTiO}_4)^{2-}$ and $(\text{SrTiO}_2)^{2+}$ layers. If nothing is done to counter this effect, one obtains two charged dislocations, a configuration that we found to be highly unstable. This instability stems from the large dipole that the two charged dislocation cores introduced into the system. The solution to this problem, depicted in Figure 1, is to simply move two of the extra oxygen ions in the top cut (corresponding to 50% of the total number of oxygen ions in that column) to the bottom cut, thus yielding two reconstructed, nonpolar surfaces. This procedure forms two identical dislocation cores. The energy of the system is lowered by ~ 20 eV, confirming the validity of this approach in stabilizing the dislocation system. Furthermore, the dislocation structure is in agreement with that deduced from High Resolution-Transmission Electron Microscopy (HR-TEM) experiments⁶⁵ (see below). MD runs on this system maintain a stable dislocation configuration, as will be shown below.

Figure 1b shows the strain map in the relaxed system, obtained by calculating local changes in the lattice parameter (see caption for further information). As expected, we observe zones in the vicinity of the dislocation cores with high tensile and compressive strains. The spatial extent of these zones is quite small, within 1 nm, in good agreement with experimental observations.⁶ For larger distances from the cores, the system exhibits a homogeneous uniaxial strain along the y -axis (tensile in the middle of the slab, compressive in the upper and lower parts of the slab). This is because of the way the dislocations have been introduced. Since two atomic planes have been removed in the middle (see Figure 1a) and we use periodic boundary conditions, the system is uniaxially strained along the y -axis ($\langle 100 \rangle$) by $\pm 2\%$. For large distances from the cores, the material can be assumed to behave as bulk (though uniaxially strained), i.e., it is not affected by the dislocation core or its local strain field.

The dimensions of the simulation box in Figure 1 are approximately $2\text{ nm} \times 10\text{ nm} \times 20\text{ nm}$ (corresponding to $\sim 40\,000$ atoms). This means that the dislocation cores are separated by $\sim 10\text{ nm}$ along z -axis ($\langle 011 \rangle$ direction), which we find to be sufficient to treat each dislocation as independent (see strain map in Figure 1b, and also the results below). The vacancy formation energy is converged at this size of the simulation model, which was proven by comparing with larger systems. When performing MD calculations for local diffusion coefficients, larger systems, $8\text{ nm} \times 10\text{ nm} \times 20\text{ nm}$ (160 000 atoms), are simulated to obtain better statistics. The diffusion coefficients were averaged over up to 5 independent simulations for those cases in which the diffusion was slow (see Section 3.3.1).

3. RESULTS

3.1. Validation of the Dislocation Model in SrTiO_3 .

Previous work has already shown that the Thomas potential for SrTiO_3 can accurately describe both the bulk structural and conducting properties^{49–51} of SrTiO_3 , and the core structure^{52,53} of the $\langle 110 \rangle \{110\}$ edge and screw dislocations. Here we focus on the $\langle 100 \rangle \{110\}$ edge dislocation, which structure has been experimentally characterized in the literature.^{2,12,65} In Figure 2, we report the simulated core structure. We remind the reader that both dislocations are identical by construction, so our description applies to either core. The dislocation core has a characteristic trapezoidal shape (highlighted by a yellow trapezoid). The TiO_2 plane at the core splits into half-filled columns of Ti and O (indicated by the top arrow splitting into two arrows), thus matching the structural pattern in the compressive zone. The split O columns at the top part (highlighted by a red rectangle in Figure 2b) have only two

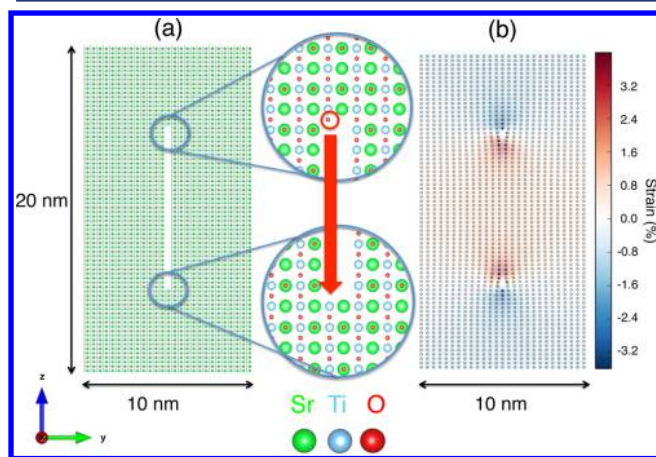


Figure 1. (a) Schematic of the procedure used to construct two opposite dislocations. First the box is rotated so that the x , y , and z axes correspond to the $\langle 0\bar{1}1 \rangle$, $\langle 100 \rangle$, and $\langle 011 \rangle$ crystallographic directions. A cut is then introduced in the middle of the box by removing an SrO and a TiO_2 plane. To avoid having charged dislocation cores, half the oxygen atoms are moved from one core (top) to the other (bottom) shown by the red circle and arrow, to ensure that both surfaces are nonpolar. The system is then relaxed, and the cut heals and two identical dislocations are created. (b) Strain map for the equilibrated system, obtained by calculating the local changes in the cation separation distances, $\Delta d_{\text{Sr-Sr}} = (d_{\text{disl}} - d_{\text{bulk}})/d_{\text{bulk}}$, where d_{disl} and d_{bulk} are the Sr–Sr bond distances in the model with a dislocation and in the unstrained dislocation-free bulk model, respectively, as done in previous work.²² Circles in (b) are the Sr atom positions, while Ti and O are not shown for the sake of clarity. Tensile (red) and compressive (blue) zones can be observed, especially in the vicinity of the dislocations.

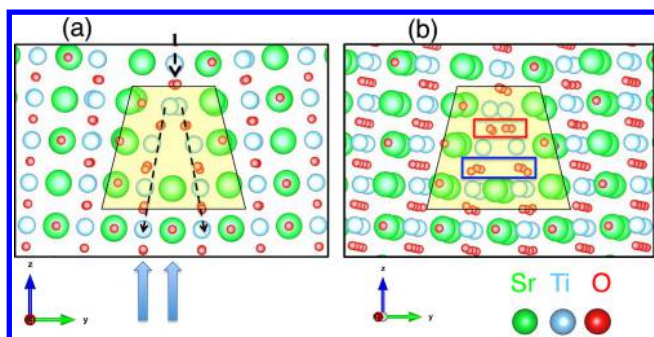


Figure 2. Dislocation core structure obtained from the static relaxation calculation. (a) Front view with the x -axis perpendicular to the screen direction; (b) the same structure rotated around z , showing the structural vacancies on the oxygen columns at the dislocation core. The large blue arrows from the bottom in (a) point to the SrO and TiO₂ planes that have been removed on the top part of the image to create the dislocation. Dashed arrows from the top are a guide to the eye for the splitting of the Ti and O columns, as discussed in the text. The red and blue rectangles in (b) indicate the O columns that have reduced occupancy, with 50% and 25% of structural oxygen vacancies per column, respectively.

oxygen atoms out of four. The O columns at the bottom are both missing one oxygen atom out of four (highlighted by a red rectangle in Figure 2b). These missing oxygen atoms therefore constitute structural vacancies, at 50% and 25% in the top and bottom part of the core, i.e., they are present even if the SrTiO₃ model, as a whole, is stoichiometric and their importance will be highlighted in Section 3.3.

Comparison of our simulated core structure of the $\langle 100 \rangle \{011\}$ edge dislocation in SrTiO₃ with the HR-TEM data of Jia et al. (see Figure 3 of ref 65) shows that the simulated structure contains all the salient features of the experimentally imaged dislocation; i.e. the trapezoidal shape of the core, the splitting of TiO₂ planes and the reduced occupancy of these columns because of their splitting at the dislocation core. The experimental diagram shows a slightly more disordered structure than the simulated one, e.g. some oxygen columns split into four columns at the core. This is probably due to the fact that we are starting with an ideal stoichiometric system during the construction of the model, as shown in Figure 2, while the structure in ref⁶⁵ might contain impurities and oxygen vacancies.^{65,66} We also note that some atomic columns in ref⁶⁵, especially in the case of Sr, have reduced occupancy, while we do not observe this feature in the simulated stoichiometric model. Again, this might be due to local changes in the material's composition and stoichiometry, though the authors also suggest that it might be due to limitations of the experimental technique.⁶⁵

In summary, the validated structure of the $\langle 100 \rangle \{011\}$ edge dislocation core in SrTiO₃, together with the extensive validation of the Thomas potential performed by other groups,^{49–56} makes us confident that this interionic potential is suitable to assess the defect chemistry and transport properties along the dislocation in SrTiO₃. We have performed further tests of the accuracy of this potential for bulk ionic conductivity, chemical expansion and vacancy formation energies of SrTiO₃, which can be found in section 1 in the Supporting Information.

3.2. Effects of the $\langle 100 \rangle \{011\}$ Edge Dislocation on the Defect Chemistry. In this section, we assess the defect chemistry in the vicinity of the $\langle 100 \rangle \{011\}$ dislocation in

SrTiO₃. SrTiO₃ crystallizes in the densely packed perovskite structure, so the only type of point defects found in this material is vacancies on all three sublattices.^{12,67} Here we focus on oxygen vacancies only, because they are relevant to the goal of this paper, and are energetically the most favored type of point defect under most conditions.⁶⁷

Our calculations show that the oxygen vacancy formation energy near the dislocation core is significantly lower than in dislocation-free bulk SrTiO₃, in the regime where the concentration of oxygen vacancies is low (ppm level). This can be seen in Figure 3, where we map the formation energy of

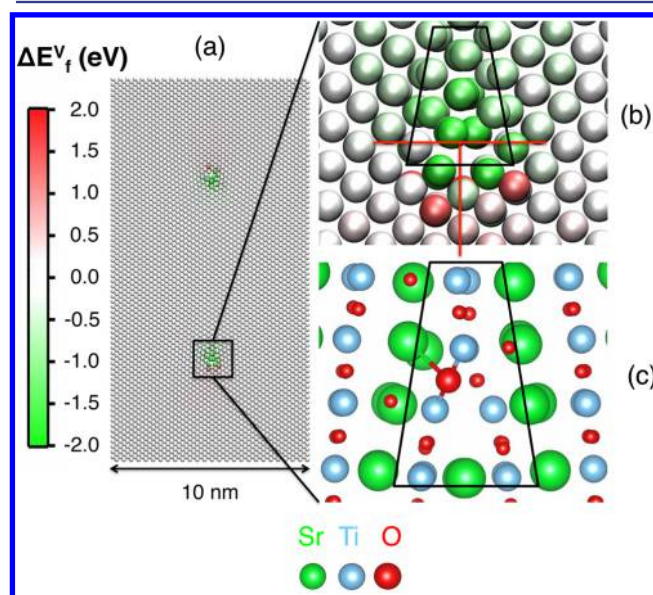


Figure 3. (a) Map of the change in the formation energy of oxygen vacancies, ΔE_f^v , for the SrTiO₃ with two dislocations relative to E_f^v obtained for bulk dislocation-free SrTiO₃. Only the oxygen atoms are shown and these are color coded according to ΔE_f^v . (b) ΔE_f^v map for one of the dislocation cores shown more closely. Oxygen atoms in the vicinity of the core have significantly lower vacancy formation energies (shown in green). (c) Atomic structure of the dislocation core. Each oxygen atom at the core is coordinated to only 3 cations, while the oxygen coordination in bulk SrTiO₃ is 6. Green, azure, and red spheres are Sr, Ti, and O atoms, respectively.

a single oxygen vacancy (corresponding to a concentration of 0.004%) in the SrTiO₃ model with two edge dislocations. In this map we show only the oxygen ions (Sr and Ti cations are hidden for simplicity) and we color-code these ions according to the change in their vacancy formation energy, ΔE_f^v , with respect to E_f^v obtained for bulk dislocation-free SrTiO₃, similar to the approach used by Uberuaga and Benedek.⁵⁴

Figure 3a shows our entire simulation box; most of the oxygen atom sites are white/gray, meaning that the energy required to remove them is similar to that in bulk SrTiO₃. A closer look at these atoms (away from the dislocations) shows that their formation energy is actually slightly higher/lower in the compressive/tensile uniaxially strained parts of the model compared to bulk dislocation-free SrTiO₃, the difference being small, ~ 0.2 eV. Lattice strain has been shown to affect the vacancy formation energy of several metal-oxide materials,^{68,69} with tensile/compressive strain favoring/hindering vacancy formation (see also Supporting Information Figure S3). This factor explains the relatively small difference (~ 0.2 eV) in the formation energy of oxygen vacancies away from the dislocation

core. On the other hand, the formation energy of oxygen vacancies close to the dislocation core (Figure 3b) varies significantly from the bulk value. Indeed, most of the oxygen sites at the dislocation core (highlighted by the black trapezoid) have vacancy formation energies that are up to 2.0 eV lower than in bulk. Conversely, some of the oxygen sites in the compressive part of the dislocation, next to the core, have higher vacancy formation energies (up to 1.5 eV higher than bulk). Our results are in good agreement with the evidence from Electron Energy Loss Spectroscopy (EELS) measurements that have shown that SrTiO_3 is oxygen deficient at the dislocation core,^{2,12,65,66} and with previous calculations on MgO ⁷⁰ and SrTiO_3 .²⁰ The changes in the formation energy for oxygen vacancies at the dislocation core can be explained in terms of the local coordination environment of the oxygen ions. The oxygen ions at the dislocation core are under-coordinated—many have a coordination number of only 3, i.e., half of the coordination expected in bulk SrTiO_3 (see Figure 3c). This under-coordination (i.e., the fact that there are fewer bonds to break) lowers the oxygen vacancy formation energy for these positions. This is conceptually similar to the behavior of oxide ions at the surface and/or grain boundaries, where the oxygen vacancy formation energy is also found to be lower.^{54,71–75}

Figure 3b shows that it is energetically favorable to create one oxygen vacancy at the core of stoichiometric SrTiO_3 . Next, we focus our attention on how many vacancies can actually be accommodated in this dislocation, i.e. how the vacancy formation energy changes with increasing amount of oxygen vacancies at the core. We find that *a maximum of 3 oxygen vacancies (for this size of the model) can be created at the core before the bulk starts reducing*, which corresponds to a vacancy concentration of $\sim 8.0\%$ at the core. To estimate this, we proceeded as follows. We removed from each core one oxygen atom at the site with the lowest vacancy formation energy, that is shown in Figure 3. We then recalculated the formation energy map for this slightly oxygen-deficient system. Figure 4b shows that it is still favorable to create the next oxygen vacancy at the core. The reduction in vacancy formation energy, with respect to bulk, is 1.3–1.6 eV (in the previous case it was ~ 2.0 eV). We repeated this procedure until we found that removing oxygen atoms from the core is no longer energetically favorable compared to bulk (i.e., away from the dislocations). We found that no more than 3 vacancies per core can be created (Figure 4d) in our system. We define the core as a circle of radius 0.4 nm, i.e., about one unit cell lattice parameter of SrTiO_3 (see Figure 4a). There are 37 oxygen atom sites in this region, which means that 3 vacancies correspond to 8.0% vacancy concentration at the core. This result can be interpreted as follows: if one starts reducing this material by slowly lowering the $p\text{O}_2$ while equilibrating the system, one would reach a vacancy concentration of 8.0% at the dislocation core before the bulk of the material starts reducing. Supporting Information section 4 reports an estimate of how many vacancies can be accommodated at the dislocation cores of a SrTiO_3 sample as a function of the dislocation density. We stress that our calculation of concentration is based on formation energies only and neglects any entropic or phonon contributions or kinetic effects.

We note that the formation energy maps deduced here impact the first term, that is the concentration term, in eq 1 for the diffusion coefficient. Space-charge effects have been invoked in the interpretation of oxide ion and electronic conductivity

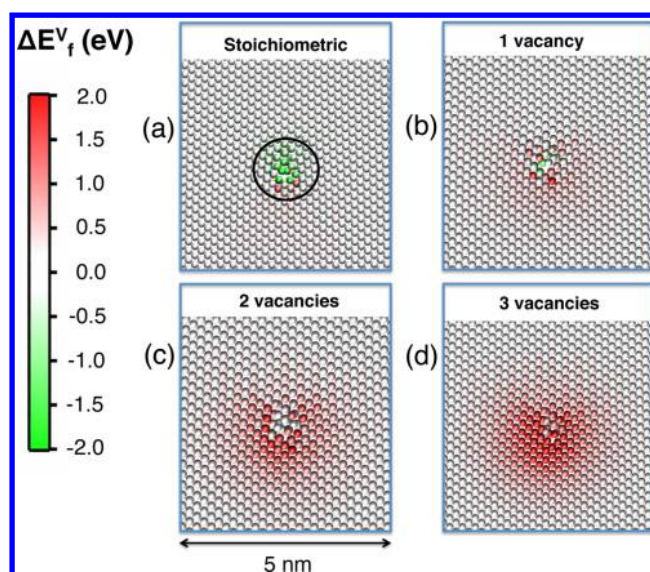


Figure 4. Relative formation energy ΔE_f^V maps of a single oxygen vacancy in stoichiometric SrTiO_3 (a), in SrTiO_3 with 1 vacancy per core (b), in SrTiO_3 with 2 vacancies per core (c), and in SrTiO_3 with 3 vacancies per core (d). The lowest formation energy in each model is lower than the bulk value by (a) 2.0, (b) 1.6, (c) 0.8 eV. The circle in (a) has a radius of 0.4 nm (see also text).

studies in SrTiO_3 .^{20,74,76,77} Here we assess the formation of a space-charge zone around the dislocation based on the formation energy of oxygen vacancies. In Figure 5a, we show the relative formation energy map of an oxygen vacancy in the SrTiO_3 model with 3 vacancies per core. This is the same result as the one shown in Figure 4d, though the color scale and lateral size have been changed for clarity. The presence of oxygen vacancies at the dislocation core causes a depletion zone for oxygen vacancies around the dislocation (red/white region). In this depletion zone, which extends to a few nanometers (3–5 nm), the creation of a new vacancy costs at least 0.3 eV more than in the bulk away from the dislocation. From the data in Figure 5a, one can extract the expected vacancy concentration distribution using the following formula:

$$[V_{\text{O}}^{\bullet\bullet}] = [V_{\text{O}}^{\bullet\bullet}]_0 \exp[-(\Delta E_f^V)/k_B T] \quad (4)$$

where $[V_{\text{O}}^{\bullet\bullet}]_0$ is the bulk vacancy concentration, corresponding to $1.27 \times 10^{19} \text{ cm}^{-3}$ (6 vacancies in a model size of $22.1 \text{ \AA} \times 105.6 \text{ \AA} \times 204.6 \text{ \AA}$) for the system in Figure 5a. This vacancy concentration profile is shown in Figure 5b as a function of distance from the dislocation core at 1000 K. As expected, a strong vacancy depletion is observed in the vicinity of the core, and the bulk vacancy concentration is only recovered 4–5 nm from the core. We note that the presence of two bands at slightly larger and smaller values than $[V_{\text{O}}^{\bullet\bullet}]_0$ is due to the slightly different formation energy in the uniaxially tensile and compressive strained regions away from the dislocation core, respectively (see also caption of Figure 5). The space-charge profile of Figure 5b can be explained as follows. Positively charged oxygen vacancies accumulate at the core, because its under-coordinated structure makes it energetically easier to create vacancies. However, this accumulation of vacancies imparts a net positive charge at the core, and electrostatically repels other positively charged oxygen vacancies in the neighboring region. In effect, this is the formation of a space-charge zone around the dislocation, predicted and visualized

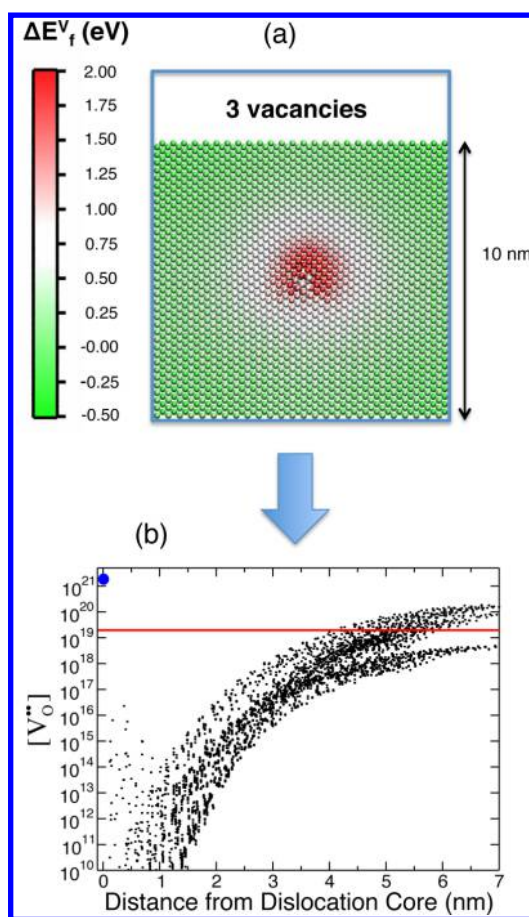


Figure 5. (a) Relative formation energy ΔE_f^V for the same model reported in Figure 4d, but with a different color scale (between -0.5 and 2.0 eV) and larger lateral size, to more clearly see the extent of the space-charge region around a nonstoichiometric dislocation core. (b) Vacancy concentration vs distance from the dislocation core, as calculated from eq 4 at 1000 K. The red horizontal line indicates the bulk concentration, $[V_O^{••}]_0 = 1.27 \times 10^{19}$ cm⁻³ (assuming the vacancies in the entire model are randomly distributed, as a reference value), while the blue circle at 0 nm indicates the vacancy concentration in the vicinity of the core (3 vacancies, see Figure 4), corresponding to 3.94×10^{21} cm⁻³. We note that, because of the uniaxial tensile and compressive strain present in regions away from the dislocation (see Figure 1), the formation energy in these regions is slightly larger or smaller than in the unstrained bulk SrTiO₃ (see Figure 3 and following discussion). For this reason $[V_O^{••}]$ away from the dislocation shows two bands that plateau at higher and lower values than $[V_O^{••}]_0$ in the uniaxially tensile and compressively strained zones of the simulation model, respectively.

from the atomistic scale, when the only charged defect is oxygen vacancy in SrTiO₃, where the electrons are treated to be totally delocalized over all the Ti and O ions (see Section 2). We also note that the quantitative result in Figure 5 is valid for the given concentration of oxygen vacancies, and one should expect a different result depending on the concentration, for example a weaker space-charge zone with increasing concentration of oxygen vacancies.

A similar behavior to that reported in Figure 5 has been observed experimentally by De Souza et al. at the surface of SrTiO₃.^{20,74,76} By performing ¹⁸O exchange and tracer diffusion experiments, the authors have found evidence of vacancy depletion near the surface of SrTiO₃; this layer extends over 5–30 nm beneath the surface, depending on several experimental

factors, such as the surface termination and morphology. This value appears larger than the spatial extent predicted in Figure 5b. One reason for this difference is that the employed potential significantly underestimates the dielectric constant of SrTiO₃ in this work (a well-known and unavoidable shortcoming of rigid-ion potentials⁴⁹). Knowing that the space-charge length is proportional to the square root of the dielectric constant,^{76,78} one can rescale our predicted spatial extent of the charge separation by $(\epsilon_{\text{exp}}/\epsilon_{\text{calc}})^{1/2} = 7.9$, where ϵ_{exp} and ϵ_{calc} are the experimental and calculated dielectric constants, respectively (see Supporting Information Section 1.5). This scaling increases our predicted depletion region from 4–5 nm to 32–40 nm, which is in good agreement with the experimental results of De Souza et al.,⁷⁴ and with the range 32–56 nm calculated by using eq 23 of ref⁷⁶ (here we used the experimental dielectric constant, 300, and a space-charge potential in the 0.4–0.8 eV range, in agreement with refs^{20,74}). Finally, we point out that the presence of such a heterogeneous concentration profile of vacancies can have a significant effect on the electrical (ionic and electronic) conductivity^{20,74} of this material (see eq 1), a point that will be discussed in the next sections.

3.3. Effects of the $\langle 100 \rangle \{011\}$ Edge Dislocation on the Oxide-Ion Conductivity. We now turn our attention to the effect of dislocations on the oxide-ion conductivity in SrTiO₃. We study two different regimes of vacancy concentration. The first one is a low vacancy concentration (dilute) regime, with an overall vacancy concentration of 0.017%, corresponding to approximately 200 ppm. This is equivalent to having fewer vacancies than the maximum number that is favorable to form at the dislocation core compared to the bulk (see Figure 4). This dilute regime is relevant to resistive-switching applications of SrTiO₃. The second regime has a significantly higher vacancy concentration, in the range of 0.5–2.5%. In this case, the total number of vacancies is several orders of magnitude higher than what can be accommodated favorably at the dislocation core that is shown in Figure 4. We note here that such high vacancy concentrations can only be achieved at high temperatures and low pO₂, or by doping, and are therefore more relevant to applications such as fuel cells, separation membranes, catalysis or sensors.

3.3.1. Low Vacancy Concentration Regime (~200 ppm). In the low vacancy concentration regime (0.017%), we assess two different cases. In the first case (sample I), the starting configuration is taken from Figure 4c, i.e., vacancies are already in their most stable position at the dislocation core. In the second case (sample II), the vacancies are randomly distributed in the material. In principle, these two cases should yield identical results because the vacancy distribution in sample II should equilibrate to the lowest energy configuration predicted in Figure 4, unless kinetic effects play a role in the limited time-scale of MD simulations, as discussed later.

Figure 6a shows the different regions of the SrTiO₃ simulation model from which we extract diffusion coefficients. These are the one-dimensional diffusion coefficients along the dislocation (denoted as D_x), which allows us to assess whether there is fast pipe diffusion. Our calculations show that the diffusion coefficients along the other directions (D_y and D_z) are smaller than those of the bulk, as recently also observed in our work on ceria.²² The computed diffusivity along the dislocation, D_x , is normalized by the one-dimensional diffusivity in the bulk dislocation-free SrTiO₃ model, with the same concentration of oxygen vacancies and at the same temperature.

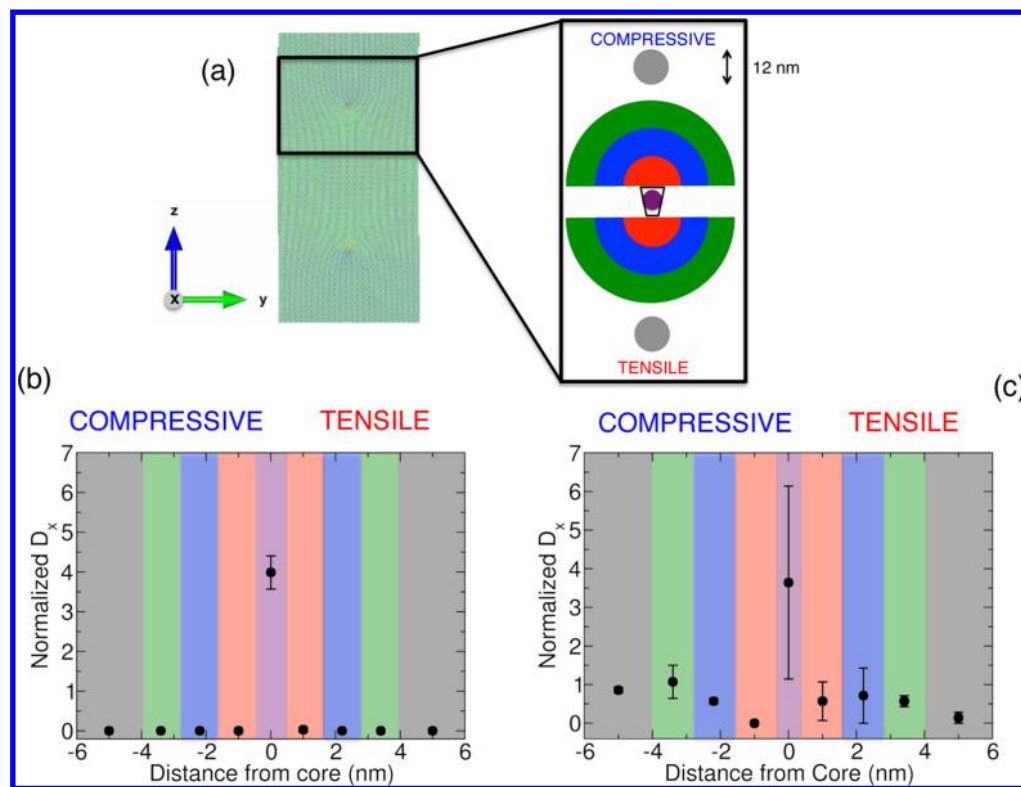


Figure 6. (a) Schematic of the different regions used for the calculation of the local diffusion coefficients in SrTiO₃ along the dislocation line. The dislocation core is shown as a black trapezoid. We define one cylindrical region (purple) of radius 0.4 nm as the dislocation core. We then define 6 semicylindrical regions, 3 in the tensile (red/blue/green bottom regions) and 3 in the compressive (red/blue/green top regions) parts of the simulation model. Finally, two bulk regions are defined (gray cylinders) 5 nm away from the dislocation, one in the uniaxial tensile and one in the uniaxial compressive part. Normalized D_x in sample I (b) and sample II (c) vs average distance from the core are plotted for different regions shown in (a). The data was obtained by averaging over 5 independent calculations for sample I and 3 for sample II. Error bars are the standard deviation from the different runs and in most cases are smaller than the symbol size. In both plots D_x is normalized by the one-dimensional diffusivity in the bulk dislocation-free SrTiO₃ model and the total vacancy concentration is 0.017%. The simulations were performed at 1200 K and were 20–30 ns long.

Our results show that the diffusion coefficient varies significantly from one region to another for sample I, in which the starting vacancy distribution is taken from that in Figure 4c. This is shown in Figure 6b that reports the normalized D_x at 1200 K, plotted versus the average distance of the studied region with respect to the dislocation core. Negative/positive distances are used to indicate the compressive/tensile parts of the model. First, we note that most of the calculated diffusion coefficients in sample I are equal to zero, within the statistical error. The only diffusion coefficients that are nonzero are either in the dislocation core region or in the tensile region next to the dislocation core (the latter being very small, see Table 1). Analysis of the vacancy positions (see Supporting Information Figure 5) reveals that vacancies reside in the vicinity of the dislocation cores and never move away from them during the 30 ns of MD simulation. This is consistent with the findings summarized in Figure 4, which shows that there is a significant energy gain for vacancies to be at the dislocation core. Second, we observe that the diffusion coefficient at the core of the dislocation is larger than that of dislocation-free bulk SrTiO₃, by a factor of ~ 4.0 , which is quite significant. While this might look like evidence for pipe-diffusion along the dislocation, below we demonstrate that this is not the case.

We now compare our results to the experimental data available in literature. Only the work of Szot et al.⁴⁷ provides an

Table 1. Calculated Diffusion Coefficients in SrTiO₃ with 0.017% Vacancy Concentration in Sample I (with an Equilibrated Distribution of Vacancies) at 1200 K^a

distance from core (nm)	D_x or D (10^{-10} cm ² /s)
−0.4 → 0.4	5.6 ± 0.6
0.4 → 1.6	0.04 ± 0.08
Core of stoichiometric SrTiO ₃ (−0.4 → 0.4)	6.2 ± 4.8
Dislocation-free bulk SrTiO ₃	1.40 ± 0.07
Dislocation core (from ref 47 at 1073 K)	0.1
Bulk (from ref 47 at 1073 K)	10^{-5}
Bulk (from ref 74 at 1073 K)	0.2
Bulk (from ref 79 at 1073 K)	10

^aWe only report those values that are non-zero along the dislocation line, D_x . Errors are estimated from the standard deviation of the values obtained from 5 and 2 independent calculations for sample I and for the stoichiometric SrTiO₃, respectively. Values for the bulk diffusion coefficient, D , from a simulation of stoichiometric SrTiO₃ and from several experiments^{47,74,79} are also reported.

estimate of both the bulk and dislocation diffusion coefficients at 1073 K in SrTiO₃, from an ¹⁸O tracer diffusion experiment. Indeed, our calculated D_x values for the dislocation are in the $(5.6-0.04) \times 10^{-10}$ cm²/s range at 1200 K (see Table 1), which is in reasonable agreement with Szot's finding of 0.1×10^{-10} cm²/s (considering our calculations are at a higher temperature by 127 K). Table 1 also reports the experimental values from

various reports for the bulk diffusion coefficient of SrTiO_3 , but these span 6 orders of magnitude, thus making a comparison hard.

To pin down the origin of the higher diffusion coefficient at the dislocation core, we consider two possible factors, as described in eq 1. First is increased mobility, which should be reflected by lower migration energies. Second is increased vacancy concentration, as noted above and in Figure 4. We performed static NEB calculations to estimate the migration barrier of an oxygen ion diffusing along the dislocation. These barriers have been calculated by introducing one oxygen vacancy in either column 1, 2, or 3 (see Figure 7), and then

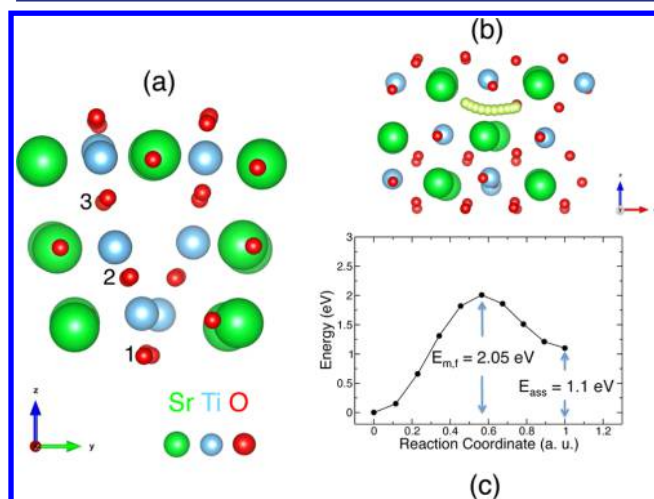


Figure 7. (a) Dislocation core structure in which we highlight the three oxygen columns used for the calculations summarized in Table 2. (b) Migration trajectory of one oxygen atom along column 3 (light yellow). Note that the image in (a) has been rotated around z in (b) to show the diffusion path along the x -axis (the dislocation line) in-plane. (c) Minimum energy path for the trajectory shown in (b), calculated by the nudged elastic band method.

calculating the energy barrier for a neighboring oxygen atom to migrate to this vacant site. These jumps were found to have different migration barriers depending on the vacancy position along the column because of the asymmetric environment around the dislocation. We therefore surveyed all these migration pathways and report only the highest barrier measured per each column along the dislocation (Table 2). We note that, since oxide ion diffusion involves a series of consecutive hops of an oxide ion along the column, the hop

Table 2. Migration Barriers Calculated from Nudged Elastic Band Calculations^a

column	$E_{m,f}$ (eV)	$E_{m,b}$ (eV)	E_{ass} (eV)
1	1.02	0.0	1.02
2	2.05	0.15	1.9
3	2.00	0.90	1.1
Dislocation-free bulk	0.90	0.90	0.0

^aFor the sake of simplicity, we report here only the largest-barrier-path calculated along each column. $E_{m,f}$, $E_{m,b}$, and E_{ass} are the forward, backward, and association energies for a given path, as explained in the text. Note that even though we are reporting the forward and backward migration barriers for each path, the diffusion will be limited by the higher barrier since equivalent paths are connected in series along the dislocation.

with the highest energy barrier is the rate-limiting step for diffusion along the dislocation.

Our results (summarized in Table 2 and Figure 7) clearly show that the migration energies at the core are higher than in bulk SrTiO_3 , so that the concept of pipe diffusion with a higher mobility for oxygen is not valid along the dislocation in SrTiO_3 . As an example, in Figure 7b,c, we report the migration trajectory and the minimum energy path (MEP), respectively, of an oxygen ion diffusing along column 3. We note that the trajectory is curved, which is consistent with the well-known path shape for oxygen migration in perovskite oxides.^{80,81} The MEP has two key features. First, the migration energy barrier (2.00 eV) is significantly higher than the value calculated in dislocation-free bulk SrTiO_3 (0.90 eV). Second, the initial and final points have different energies, meaning that vacancies prefer to reside in, or are preferentially bound to, certain sites along the column. This preference is because different oxygen atoms in the same columns have different coordination environments (e.g., cation-oxygen bond distances change significantly from one site to another), making certain sites more favorable than others. The difference between the initial and final energy that represents the association energy is reported in the last column of Table 2. Such large association energies (up to 1.9 eV) increase the total migration energy and therefore hamper the oxygen diffusion, especially at lower temperatures, as observed in other ionic conductors.^{48,63,82}

Next, we consider sample II, in which vacancies are randomly distributed at the start of the simulation. Like in the case of sample I, we observe the highest diffusion coefficient at the dislocation core. However, sample II also shows nonzero diffusion coefficients in several other regions, both in the compressive and tensile part, with no clear trend between the magnitude of the diffusion coefficient and distance from the core (see also Section 3.3.2). An analysis of the vacancy positions explains this behavior. After 20 ns, most vacancies are still randomly distributed in the material and have not moved to the dislocation core to equilibrate. Those regions that contain oxygen vacancies are the ones that show oxide-ion diffusivity. Sample II therefore seems to be in a metastable state in which vacancies have not reached their equilibrium distribution (that favors them to be all at the core, as in Figure 4 and sample I). To better understand the metastability of sample II, we estimate the average distance, l , traveled by a vacancy using the following formula:

$$l = \sqrt{D_V t}, \quad (3)$$

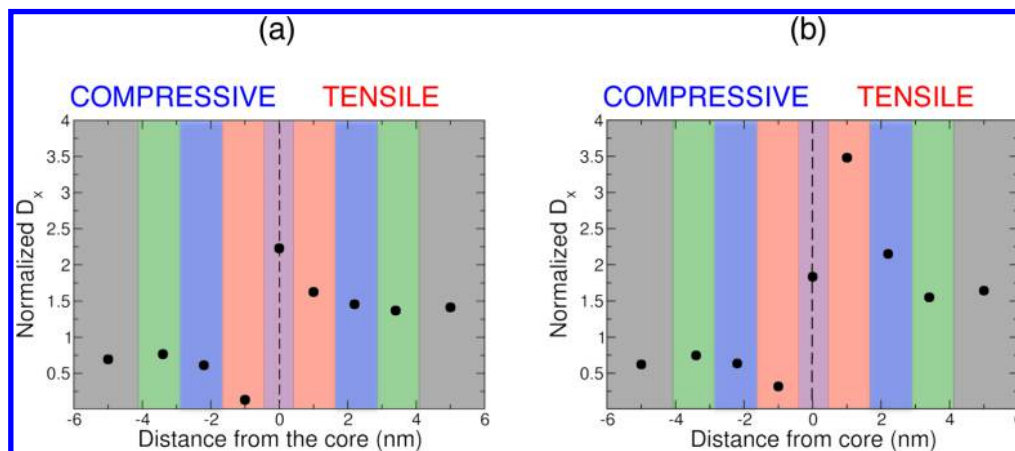
where D_V is the vacancy diffusion coefficient (related to the oxygen diffusion coefficient via $D_V[\text{V}_\text{O}^\bullet] = D_\text{O}[\text{O}]$) and t is the time. Using the data from our calculations (reported in Table 3), we obtain $l = 1.3$ nm on sample II for $t = 20$ ns. This distance is not sufficient to achieve an equilibrium vacancy distribution in our large system (the average vacancy–vacancy distance is 5 nm). Furthermore, we note that because of the depletion zone around the core (red area in Figure 5a), the diffusion of vacancies into the core might be further hampered and therefore l might be significantly smaller than what we predict here (see also discussion on space-charge in previous section).

On the other hand, under typical experimental time-scales (1 h) at room temperature, l is in the range of 10^3 – 10^5 nm (again neglecting the effects of the vacancy depletion zone around the dislocation). This is significantly larger than the average dislocation–dislocation distance extracted from the data in

Table 3. Average Distance, l , Travelled by an Oxygen Vacancy in SrTiO₃ in Our Simulations and in an Experiment at Room Temperature^a

system	D_O (10^{-10} cm ² /s)	D_V (10^{-10} cm ² /s)	time, t (ns)	distance, l (nm)
0.017% [$V_O^{\bullet\bullet}$] @ 1200 K (MD simulation in this work)	1.4	8400	20	1.3
0.017% [$V_O^{\bullet\bullet}$] @ 300 K (typical experimental conditions)	10^{-2} – 10^{-4} from refs 47, 74, 79	10 – 10^{-1}	3.6×10^{12}	10^3 – 10^5
2.5% [$V_O^{\bullet\bullet}$] @ 1200 K (MD simulation in this work)	14.7	588	20	0.34

^aWe note that the experimental diffusion coefficients are obtained by extrapolating high-temperature data, as done in ref 37.

**Figure 8.** Calculated normalized diffusion coefficient along the direction of the dislocation line, D_x , as a function of average distance from the core for 0.5% vacancy concentration (a), and for 2.5% vacancy concentration (b). These calculations were performed at 1200 K and the simulations were run for 5–20 ns. See Figure 6a for the schematic of regions in which D_x was calculated.

ref⁴⁷ (~ 160 nm) and is comparable to that of the annealed single crystal SrTiO₃ samples (~ 1300 nm), as in ref 83. Therefore, under experimental conditions (i.e., dislocations introduced into the specimens, for example, by mechanical deformation, and kept at room temperature for extended periods), we expect the situation along dislocations to be closer to the case of sample I (equilibrated). But how many vacancies then remain in the bulk (zones away from the dislocation) depends on the dislocation density of the specimen, the vacancy concentration (see also section 4 in Supporting Information), the temperature and time and will affect the total bulk diffusion coefficient.

A final interesting observation is that we find some oxide ion diffusion along the dislocation core even when SrTiO₃ is stoichiometric. Indeed, when simulating fully stoichiometric SrTiO₃ (1200 K for 30 ns), we calculated a diffusion coefficient, D_x , of 6.2×10^{-10} cm²/s for the dislocation core (this value was obtained as an average over two independent calculations), a value of the same order of magnitude of that calculated along the dislocation of sample I (see Table 1). In all the other regions, no diffusion was observed because of lack of vacancies. Figure 2b provides an explanation for this otherwise unexpected result. Indeed, because of the way a dislocation is formed, some oxygen columns at the dislocation core have a reduced occupancy, even if the system is stoichiometric. These structural vacancies are therefore responsible for the observed oxide-ion diffusion at the dislocation core even when SrTiO₃ is fully stoichiometric. NEB calculations confirmed this finding by showing that oxygen migration through these structural vacancies is possible, though the migration energy is high (1.7–2.2 eV).

In summary, the results in Figure 6 and Table 1 clearly show that the oxygen diffusion coefficient can be strongly heterogeneous in sample I. This is because, for low vacancy

concentrations, SrTiO₃ tends to accumulate most of the vacancies in the vicinity of the dislocation cores (which show significant oxygen diffusion), while the remainder of the material is left stoichiometric (thus with no oxygen diffusion). A consequence of this is that dislocations are oxygen-deficient, as indeed observed in refs.^{2,12} The resulting oxygen diffusion coefficient along the dislocation is then higher than that in the dislocation-free bulk SrTiO₃ because of an increased oxygen vacancy concentration (i.e., [$V_O^{\bullet\bullet}$] in eq 1), and not because of an increased mobility (i.e., $\exp(-E_m/k_B T)$ in eq 1) at the dislocation.

3.3.2. High Vacancy Concentration Regime (0.5% and 2.5%). We now turn our attention to the role of dislocations on the oxide-ion mobility for SrTiO₃ with relatively high vacancy concentrations. Here we investigate SrTiO₃ with 0.5% and 2.5% vacancy concentration, respectively. This is a significantly higher concentration of oxygen vacancies than considered before and the number of vacancies considered here is a lot higher than what can be accommodated at the core, according to the results in Figure 4. So we expect the vacancy distribution to be relatively homogeneous and the resulting diffusion coefficients to behave differently from what we found above for the dilute regime.

In Figure 8 we show the normalized diffusion coefficient, D_x , for different zones of SrTiO₃ for 0.5% (a) and 2.5% (b) vacancy concentration, respectively. The behavior for the two vacancy concentrations is quite similar, so here we can make a series of general observations that are relevant to both plots. First, at large distances from the dislocation core, the material is uniaxially strained along the y -axis, as explained in section 2.2 and Figure 1. For this reason the diffusion coefficients in the tensile/compressive parts are higher/lower than in the bulk dislocation-free SrTiO₃, resulting in normalized D_x values that are smaller/greater than 1. This is in good agreement with our

calculation in bulk dislocation-free SrTiO_3 that is uniaxially strained along the y -axis (see Table 4), and with recent work

Table 4. Oxygen Diffusion Coefficients along the Dislocation Line Direction, D_x , at 1200 K and Migration Energies of 2.5% Oxygen-Deficient SrTiO_3 , for the Different Zones As Shown in Figure 8^a

distance from core (nm)	D_x ($10^{-10} \text{ cm}^2/\text{s}$)	E_m (eV)
-5.6 \rightarrow -4.4	9.2	0.99 ± 0.05
-4.0 \rightarrow -2.8	11.0	1.01 ± 0.05
-2.8 \rightarrow -1.6	9.3	1.0 ± 0.05
-1.6 \rightarrow -0.4	4.7	1.02 ± 0.05
-0.4 \rightarrow 0.4	27.0	0.87 ± 0.05
0.4 \rightarrow 1.6	51.2	0.77 ± 0.05
1.6 \rightarrow 2.8	31.6	0.87 ± 0.05
2.8 \rightarrow 4.0	22.7	0.92 ± 0.05
4.4 \rightarrow 5.6	24.2	0.92 ± 0.05
Dislocation-free bulk	14.7	0.93 ± 0.05
Average within 1.0 nm radius from dislocation core	27.5	0.82 ± 0.05
Average within 2.2 nm radius from dislocation core	22.3	0.88 ± 0.05
Average within 3.4 nm radius from dislocation core	19.2	0.91 ± 0.05
Tensile uniaxial strained (2.5%) dislocation-free bulk	18.9	0.86 ± 0.05
Compressive uniaxial strained (2.5%) dislocation-free bulk	10.0	1.01 ± 0.05

^aThe errors associated with the diffusion coefficients are usually $\sim 5\%$, while those associated with the migration energy barriers were estimated to be ~ 0.05 eV (see section 2 of the Supporting Information for details). Migration energy barriers were calculated for runs between 1000 and 1500 K.

showing that other related oxides present a higher/lower diffusion coefficient when they are tensile/compressively strained.^{22,84–88} In the tensile part of the model, as one moves closer to the core, the diffusion coefficient increases by as much as a factor of 3.5 (Figure 8b). The opposite happens in the compressive zone, where the diffusion coefficient decreases significantly as one approaches the core. Again, this is in agreement with the common understanding that compressive/tensile strain decreases/increases the oxide ion diffusivity.^{60,84–88}

Table 4 reports the values of the diffusion coefficients shown in Figure 8b. The tensile zones that are closest to the core exhibit diffusion coefficients that are higher than the value at 5 nm away from the core (gray area, right-hand side of Figure 8b). To quantify the spatial extent of the influence of a dislocation, we averaged the diffusion coefficient over a circular region around a dislocation. The values are reported in Table 4. One can see that as the radius of this region is increased (from 1.0 to 3.4 nm), the average diffusion coefficient decreases from 27.5×10^{-10} to $19.2 \times 10^{-10} \text{ cm}^2/\text{s}$, the latter being already quite close to that of dislocation-free SrTiO_3 ($14.7 \times 10^{-10} \text{ cm}^2/\text{s}$, from MD simulations here). This means that, overall, the enhancement in the diffusion coefficient is limited to a very small region around the dislocation, and the enhancement itself is only within twice that of the bulk diffusivity.

Compared with the results shown in Figure 6, the main difference here is the more homogeneous character of the oxide-ion diffusivity. While in the dilute regime, SrTiO_3 with 0.017% vacancy concentration showed diffusion only at the

dislocation core region, SrTiO_3 with higher vacancy concentrations have finite diffusion coefficients in all the regions as shown in Figure 8 and Table 4. This is because the oxygen vacancy concentration studied here is $100\times$ larger than that of sample I and II, which is significantly more than what can be accommodated at the core. The remaining vacancies are therefore free to distribute homogeneously in the system, which has been confirmed by performing a vacancy analysis (see Supporting Information Table S3). Using eq 4, we can calculate the average distance, l (0.34 nm), traveled by a vacancy during this simulation, as done before. While this is smaller than that for sample II (1.3 nm), the $100\times$ larger vacancy concentration studied means that the vacancy–vacancy distance is significantly smaller. Indeed, one finds that there are enough vacancies within a distance l of the dislocation to completely saturate the core. We therefore conclude that the vacancy distribution of these heavily oxygen deficient compositions can be assumed to have reached equilibrium, unlike the case of sample II.

Finally, we note that we have surveyed a series of temperatures (from 900 to 1500 K) and we can confirm that in all cases the behavior is quite similar to that shown in Figure 8. In Table 4, we report the calculated migration energies for the different regions in SrTiO_3 with a vacancy concentration of 2.5%. It can be seen that the tensile/compressive zones have migration energies that are lower/higher, consistent with the diffusion coefficient data in Figure 8. The calculated migration energies in these two regions are similar to those extracted from calculations on bulk dislocation-free SrTiO_3 strained along one axis by $\sim 2\%$, which confirms the reliability of these values. The only regions that have migration energies lower than dislocation-free bulk SrTiO_3 are those tensile regions close to the dislocations. The dislocation core itself ($-0.4 \rightarrow 0.4$ nm in Table 4) has a migration energy that is essentially the same as that of dislocation-free bulk SrTiO_3 . This result is different from the higher migration energies reported for the dislocation core in Table 2 for the dilute system. However, as the name implies, in this “high vacancy concentration” regime, significantly more vacancies are present in the model than those studied in Table 2 and Figure 7. The presence of several vacancies near the core can easily change the energy landscape (in particular the binding strength of certain sites at the core), as observed in Figure 4. In conclusion, based on the results in Table 4, we do not expect a significant enhancement of the oxide ion diffusion coefficient along the dislocation line even at lower temperatures. In other words, in this regime, too, pipe diffusion with enhanced mobility of oxygen ions is not present at the edge dislocation core in SrTiO_3 .

4. DISCUSSION

The results obtained in this paper provide a thorough and atomistic understanding of the effects of an edge dislocation on the electrical and chemical properties of SrTiO_3 . In this section we discuss the implications of our results for SrTiO_3 performance in devices such as red-ox based resistive switching memories and SOFCs.

A key result of this work is that dislocation cores are more easily reduced compared to the bulk of the material. While similar observations have been made for grain boundaries and surfaces,^{20,54,71–75} this is the first time this effect is demonstrated and quantified for isolated dislocations in SrTiO_3 . We find that the main driving force is the under-coordination of the oxygen ions at the core, a feature that

dislocations share with grain boundaries and surfaces. The predicted reducibility of the dislocation is in agreement with experimental evidence showing that SrTiO_3 is oxygen-deficient in the vicinity of a dislocation core.^{2,12,65,66}

The ease of reduction at dislocation cores in SrTiO_3 has significant implications for the resistive switching behavior of this material. We note that the reducibility of the SrTiO_3 at the dislocation impacts simply and directly the thermodynamics of defect chemistry in this material, and is not driven by faster migration or oxygen exchange kinetics along the dislocation. Indeed our result actually excludes faster migration, since our calculated migration barriers at the dislocation core are higher than that in bulk. Szot et al.² recently suggested that “the extended dislocation acts as (pipe) diffusion path allowing preferential exchange of oxygen with the surroundings.” It is true, as demonstrated also by Szot et al.² that the electrical conductivity of this material under strong electric fields is determined by the electrical properties of dislocations. However, the dislocations induce local changes of electrical properties *not because of the preferably faster kinetics of oxygen exchange or migration (pipe diffusion), but simply because of the structure-driven reducibility, i.e. a thermodynamic factor.* The lower formation enthalpy of oxygen vacancies in the vicinity of a dislocation allows to reduce the SrTiO_3 preferentially along a dislocation under electric field. This reduced zone forms electronically conducting paths along the dislocation lines because of the compensating Ti d electrons released upon reduction,^{20,39,40,43} while the bulk of SrTiO_3 remains in a stoichiometric insulating state, as hypothesized by Szot et al. Our finding in this work provides an atomistic clarification for the resistive switching mechanism along dislocations in SrTiO_3 , and helps to develop more accurate and quantitative models for switching kinetics. Finally, we note that, based on our results, we expect other extended defects, e.g., grain boundaries, to play a similar role in resistive switching in SrTiO_3 , since these also show lower oxygen vacancy formation energies.^{54,75}

Another consequence of the ease of reduction at dislocation cores is the formation of a space-charge zone. As shown in Figure 5b, we were able to construct and visualize, from the atomic level, the space-charge zone around a reduced dislocation core (in the case of 8% vacancies at the dislocation core) by using the calculated formation energies shown in Figure 5a. We note the atomistic calculations here take into account both the elastic strain field around the dislocation and the electrostatic interaction between the positively charged core and the positively charged oxygen vacancies mapped around the core. In fact, it appears from Figure 5 that the electrostatic repulsion effect dominates as there is only negligible difference in the relative formation energies of oxygen vacancies between the tensile and compressive strain fields of the dislocation. These two contributions together correspond to solving the Poisson equation with an electrostatic boundary condition at an extended defect, here a dislocation, as usually done in space-charge models,^{74,76} though screening effects by other vacancies are neglected in our approach (because the only charged point defects are oxygen vacancies and the electrons are delocalized through the entire model). Here, however, we are able to retain atomistic detail and drop unrealistic assumptions such as the stepwise nature of the change in vacancy formation energy.⁷⁶ The formation of a space-charge zone has important consequences for the electronic and ionic conductivity of this material.^{20,74,76,78}

We now discuss our results on oxide ion diffusivity in the vicinity of a dislocation, a problem that has recently attracted much attention,^{5,20,22,24,70} particularly in the SOFC field, where enhancing the ionic conductivity by applying elastic strain is being considered. Here we have found a different behavior depending on the vacancy concentration. For slightly reduced (or even stoichiometric) SrTiO_3 with an equilibrated distribution of oxygen vacancies (sample I), diffusion is confined to the vicinity of the dislocation cores because of accumulation of all vacancies to the dislocation core. The regions away from the dislocation have no oxygen vacancies, therefore the diffusion coefficient is zero. However, as shown above, the increased diffusion coefficient observed at the dislocation core does not imply that the dislocations are fast pipe diffusion pathways in SrTiO_3 . NEB calculations show that migration barrier of oxygen vacancies at the dislocation core (up to 2 eV) is higher than that in dislocation-free bulk SrTiO_3 (0.9 eV), as summarized in Table 2. Furthermore, we also find strong evidence of vacancy association, i.e. the initial and final configuration of the migration pathways do not have the same energy, the difference being up to 1.9 eV. This high association energy, which effectively increases the migration barrier, is expected to severely limit the mobility of oxygen vacancies, especially at lower temperatures.⁸⁹ Since pipe-diffusion is defined as a reduction in the migration energy barrier²⁸ (E_m in eq 1), *our results provide no evidence of pipe-diffusion in SrTiO_3 .* The higher diffusion coefficient at the dislocation core is due solely to a higher vacancy concentration, i.e., a larger $[V_{\text{O}}^{\bullet\bullet}]$ and not a larger mobility, $\exp(-E_m/k_B T)$, in eq 1.

The second regime studied in this paper is when the vacancy concentration is high (0.5–2.5% range), a situation that is more relevant to SOFC applications. In this regime, vacancies are more homogeneously distributed across the material and oxide ion diffusion is observed throughout the material. The diffusion coefficients, however, do vary from one zone to the other, primarily because of the tensile and compressive uniaxial strain present in the modeled system (see Figures 1 and 8). Indeed, this can be seen in the migration energies reported in Table 4 that are lower/higher in the tensile/compressive part. The migration energy of oxide-ions in the core region is 0.87 ± 0.05 eV which is analogous to that of dislocation-free bulk SrTiO_3 (0.93 eV). This implies that no significant enhancement of the oxide ion diffusion coefficient is expected even at lower temperatures, i.e. *there is no evidence of pipe-diffusion* in this regime either. We note that the authors of this paper have recently studied another oxide material, doped CeO_2 , which also presents an oxygen-vacancy mediated conduction mechanism, and found no evidence of pipe-diffusion along an edge dislocation.²² The absence of fast diffusion along the dislocations seems therefore a common feature of these heavily reduced and/or doped oxide materials.

Finally, we would like to discuss the implications of our results for the field of fast oxide ion conductors that benefit technologies such as SOFCs, separation membranes and electrolyzers. Perovskite oxides are widely studied for these applications as materials that can serve for fast ion and electron conduction as well as for catalyzing the oxygen reduction reaction (ORR).³¹ Much research efforts have been dedicated to increase the ORR kinetics at lower temperatures (reduced from 800 °C to about 500 °C) to improve the performance of electrochemical devices.^{10,90,91} To this end, Kuklja et al. showed that the ORR kinetics in most perovskite oxides depends on the factor $D_V[V_{\text{O}}^{\bullet\bullet}]$, where $[V_{\text{O}}^{\bullet\bullet}]$ is the oxygen vacancy concen-

tration and D_V is the vacancy diffusion coefficient.⁹² Our results show that dislocations significantly facilitate the creation of oxygen vacancies (i.e., they can increase $[V_O^{\bullet\bullet}]$) in a prototypical perovskite oxide, SrTiO₃. Therefore, we suggest that a larger density of dislocations close to the material's surface might accelerate the ORR kinetics on perovskite oxides, though one would have to consider the effect of these dislocations also on surface cation composition and electronic structure.

5. CONCLUSIONS

In this paper, we assessed the role of $\langle 100 \rangle \{011\}$ edge dislocations on the defect chemistry and oxide ion transport properties of SrTiO₃ by performing atomistic simulations. We found that in SrTiO₃ oxygen vacancies close to the dislocation core have lower formation energies, by as much as 2 eV. The reason for this easier reducibility lies in the strong undercoordination of the oxygen ions at the core. Ability to map out the oxygen vacancy formation energies at the atomic scale for the case of reduced dislocation cores also allowed us to visualize the formation of a space-charge zone around the dislocation and to estimate its length to be 32–40 nm, in agreement with previous experimental work.^{20,74}

Oxide ion diffusion was studied by means of MD simulations and NEB calculations. We assessed two regimes, one with a low vacancy concentration (ppm level, relevant to resistive switching applications) and one with higher concentrations (0.5% and 2.5%, relevant to fuel cell applications). In both cases, pipe-diffusion (i.e., enhanced oxide ion mobility) is not present at the dislocation core in SrTiO₃. In the low vacancy concentration regime, however, oxygen vacancy accumulation at the core gives rise to a higher diffusion coefficient, even though the migration energy barrier is higher along the dislocation core compared to that in the bulk dislocation-free SrTiO₃. The extent of this vacancy accumulation, and thus the variation in total oxide ion conductivity, can be impacted kinetically by temperature and dislocation density.

The results reported here have important implications, especially in view of the technological importance of SrTiO₃. As reviewed by Szot et al.,² it is true that the electrical properties of dislocations control the resistive switching behavior of SrTiO₃. However, we were able to demonstrate that *dislocations induce local changes of electrical properties not because of the preferably faster kinetics of oxygen migration (pipe diffusion) as previously thought,² but simply because of the structure-driven easier reducibility.* This result is key for the resistive switching mechanism, and provides a quantitative and direct explanation for the electronic conductivity of dislocations in SrTiO₃ and related oxides studied for resistive switching. Our calculations also provided a clear atomistic picture of space charge zone around the dislocation in this material, and the same approach can be easily used for investigating space charge effects in other materials with extended defects.

Our work has also important ramifications for other fields. The absence of pipe diffusion along dislocations in SrTiO₃, an archetypical perovskite oxide, is important in quantitatively interpreting the experimental results aiming to assess the effects of strain, which sometimes include both elastic and plastic strain components, in oxide ion conductivity in oxides for energy applications. While here, and in ref 22, we demonstrated that an edge dislocation does not increase the oxide ion mobility, previous works of Kushima and Yildiz,⁸⁵ De Souza et al.,⁸⁴ and Mayeshiba and Morgan,⁸⁸ in related materials, have shown that *elastic* strain can increase the oxide ion mobility by

reducing the migration barriers. Finally, our calculations show that a larger density of dislocations close to the material's surface might accelerate the oxygen exchange kinetics on perovskite oxides, a strategy that might be worth pursuing to further enhance the performance of these materials in fuel cells.

■ ASSOCIATED CONTENT

Supporting Information

This material is available free of charge via the Internet at <http://pubs.acs.org>.

■ AUTHOR INFORMATION

Corresponding Author

*byildiz@mit.edu

Notes

The authors declare no competing financial interest.

■ ACKNOWLEDGMENTS

Authors greatly acknowledge financial support for this research from the DoE Basic Energy Sciences (DE-SC0002633). This work used the Extreme Science and Engineering Discovery Environment (XSEDE), which is supported by National Science Foundation Grant Number TG-DMR110004. This research used resources of the National Energy Research Scientific Computing Center, a DOE Office of Science User Facility supported by the Office of Science of the U.S. Department of Energy under Contract No. DE-AC02-05CH11231. We thank Dr. Mostafa Youssef on useful discussions related to defect chemistry and space charge in oxides and for calculating the dielectric constant of SrTiO₃ in this paper. We also thank Dr. Roger De Souza for clarifying some technical aspects of his previous work in modeling reduced SrTiO₃.⁵¹ and for helpful discussions on space-charge effects in this material. B.Y. would like to thank Prof. Rainer Waser for helpful discussions on oxide ion conduction along dislocations in perovskites. D.M. would like to thank Dr. Pierre Hirel for helpful discussions and sharing his amazing Atomsk software (http://pierrehirel.info/codes_atomsk.php?lang=eng) to generate and manipulate input files. D.M. thanks Alex Kohlmeyer and Steve Plimpton for support with certain functions in LAMMPS.

■ REFERENCES

- (1) Jin, L.; Guo, X.; Jia, C. L. *Ultramicroscopy* **2013**, 134, 77.
- (2) Szot, K.; Bihlmayer, G.; Speier, W. In *Solid State Physics*; Camley, R. E., Stamps, R. L., Eds.; Academic Press: New York, 2014; Vol. 65, pp 353–559.
- (3) Chen, C. H.; Kiguchi, T.; Saiki, A.; Wakiya, N.; Shinozaki, K.; Mizutani, N. *Appl. Phys. Mater. Sci. Process.* **2003**, 76, 969.
- (4) Song, K.; Schmid, H.; Srot, V.; Gilardi, E.; Gregori, G.; Du, K.; Maier, J.; van Aken, P. A. *APL Mater.* **2014**, 2, 032104.
- (5) Yildiz, B. *MRS Bull.* **2014**, 39, 147.
- (6) Chang, C.-P.; Chu, M.-W.; Jeng, H. T.; Cheng, S.-L.; Lin, J. G.; Yang, J.-R.; Chen, C. H. *Nat. Commun.* **2014**, 5, 3522.
- (7) Wang, L.; Xu, Z.; Wang, W.; Bai, X. *J. Am. Chem. Soc.* **2014**, 136, 6693.
- (8) Sneed, B. T.; Brodsky, C. N.; Kuo, C.-H.; Lamontagne, L. K.; Jiang, Y.; Wang, Y.; Tao, F. (F.); Huang, W.; Tsung, C.-K. *J. Am. Chem. Soc.* **2013**, 135, 14691.
- (9) Farmanesh, S.; Ramamoorthy, S.; Chung, J.; Asplin, J. R.; Karande, P.; Rimer, J. D. *J. Am. Chem. Soc.* **2014**, 136, 367.
- (10) Wachsmann, E.; Ishihara, T.; Kilner, J. *MRS Bull.* **2014**, 39, 773.
- (11) Trovarelli, A.; Fornasiero, P. *Catalysis by Ceria and Related Materials*, 2nd ed.; Imperial College Press: London, 2013.

- (12) Waser, R.; Dittmann, R.; Staikov, G.; Szot, K. *Adv. Mater.* **2009**, *21*, 2632.
- (13) Pijolat, C.; Pupier, C.; Sauvan, M.; Tournier, G.; Lalauze, R. *Sens. Actuators, B* **1999**, *59*, 195.
- (14) Manthiram, A. *J. Phys. Chem. Lett.* **2011**, *2*, 176.
- (15) Snaith, H. J. *J. Phys. Chem. Lett.* **2013**, *4*, 3623.
- (16) Riffat, S. B.; Ma, X. *Appl. Therm. Eng.* **2003**, *23*, 913.
- (17) Ramesh, R.; Spaldin, N. A. *Nat. Mater.* **2007**, *6*, 21.
- (18) Gao, P.; Britson, J.; Nelson, C. T.; Jokisaari, J. R.; Duan, C.; Trassin, M.; Baek, S.-H.; Guo, H.; Li, L.; Wang, Y.; Chu, Y.-H.; Minor, A. M.; Eom, C.-B.; Ramesh, R.; Chen, L.-Q.; Pan, X. *Nat. Commun.* **2014**, *5*, 3801.
- (19) Sillassen, M.; Eklund, P.; Pryds, N.; Johnson, E.; Helmersson, U.; Böttiger, J. *Adv. Funct. Mater.* **2010**, *20*, 2071.
- (20) Metlenko, V.; Ramadan, A.; Gunkel, F.; Du, H.; Schraknepper, H.; Hoffmann-Eifert, S.; Dittmann, R.; Waser, R.; De Souza, R. A. *Nanoscale* **2014**, *6*, 12864.
- (21) McKenna, K. P. *J. Am. Chem. Soc.* **2013**, *135*, 18859.
- (22) Sun, L.; Marrocchelli, D.; Yildiz, B. *Nat. Commun.* **2015**, *6*, 6294.
- (23) Dholabhai, P. P.; Pilania, G.; Aguiar, J. A.; Misra, A.; Uberuaga, B. P. *Nat. Commun.* **2014**, *5*, 5043.
- (24) Murphy, S. T.; Jay, E. E.; Grimes, R. W. *J. Nucl. Mater.* **2014**, *447*, 143.
- (25) Curtin, W. A.; Olmsted, D. L.; Hector, L. G. *Nat. Mater.* **2006**, *5*, 875.
- (26) Legros, M.; Dehm, G.; Arzt, E.; Balk, T. J. *Science* **2008**, *319*, 1646.
- (27) Huang, J.; Meyer, M.; Pontikis, V. *Phys. Rev. Lett.* **1989**, *63*, 628.
- (28) In *Diffusion in Solids*; Springer Series in Solid-State Sciences; Springer: Berlin Heidelberg, 2007; pp 583–591.
- (29) Swallow, J. G.; Woodford, W. H.; Chen, Y.; Lu, Q.; Kim, J. J.; Chen, D.; Chiang, Y.-M.; Carter, W. C.; Yildiz, B.; Tuller, H. L.; Vliet, K. J. *J. Electroceramics* **2014**, *32*, 3.
- (30) Chen, Y.; Jung, W.; Cai, Z.; Kim, J. J.; Tuller, H. L.; Yildiz, B. *Energy Environ. Sci.* **2012**, *5*, 7979.
- (31) Jung, W.; Tuller, H. L. *Adv. Energy Mater.* **2011**, *1*, 1184.
- (32) Thiel, S.; Hammerl, G.; Schmehl, A.; Schneider, C. W.; Mannhart, J. *Science* **2006**, *313*, 1942.
- (33) Mannhart, J.; Schlom, D. G. *Science* **2010**, *327*, 1607.
- (34) Muenstermann, R.; Menke, T.; Dittmann, R.; Waser, R. *Adv. Mater.* **2010**, *22*, 4819.
- (35) Jiang, W.; Kamaladasa, R. J.; Lu, Y. M.; Vicari, A.; Berechman, R.; Salvador, P. A.; Bain, J. A.; Picard, Y. N.; Skowronski, M. *J. Appl. Phys.* **2011**, *110*, 054514.
- (36) Kamaladasa, R. J.; Noman, M.; Chen, W.; Salvador, P. A.; Bain, J. A.; Skowronski, M.; Picard, Y. N. *J. Appl. Phys.* **2013**, *113*, 234510.
- (37) Messerschmitt, F.; Kubicek, M.; Schweiger, S.; Rupp, J. L. M. *Adv. Funct. Mater.* **2014**, *24*, 7448.
- (38) Ohly, C.; Hoffmann-Eifert, S.; Guo, X.; Schubert, J.; Waser, R. *J. Am. Ceram. Soc.* **2006**, *89*, 2845.
- (39) Moos, R.; Menesklou, W.; Härdtl, K. H. *Appl. Phys. A: Mater. Sci. Process.* **1995**, *61*, 389.
- (40) Balachandran, U.; Eror, N. G. *J. Solid State Chem.* **1981**, *39*, 351.
- (41) Lin, C.; Demkov, A. A. *Phys. Rev. Lett.* **2013**, *111*, 217601.
- (42) Tanaka, T.; Matsunaga, K.; Ikuhara, Y.; Yamamoto, T. *Phys. Rev. B* **2003**, *68*, 085110.
- (43) Cuong, D.; Lee, B.; Choi, K.; Ahn, H.-S.; Han, S.; Lee, J. *Phys. Rev. Lett.* **2007**, *98*, 115503.
- (44) Szot, K.; Speier, W.; Bihlmayer, G.; Waser, R. *Nat. Mater.* **2006**, *5*, 312.
- (45) Szot, K.; Dittmann, R.; Speier, W.; Waser, R. *Phys. Status Solidi RRL* **2007**, *1*, R86.
- (46) Wachsmann, E. D.; Lee, K. T. *Science* **2011**, *334*, 935.
- (47) Szot, K.; Speier, W.; Carius, R.; Zastrow, U.; Beyer, W. *Phys. Rev. Lett.* **2002**, *88*, 075508.
- (48) Kilner, J. A.; Burriel, M. *Annu. Rev. Mater. Res.* **2014**, *44*, 365.
- (49) Thomas, B. S.; Marks, N. A.; Begg, B. D. *Nucl. Instrum. Methods Phys. Res. Sect. B Beam Interact. Mater. At.* **2005**, *228*, 288.
- (50) Thomas, B.; Marks, N.; Harrowell, P. *Phys. Rev. B* **2006**, *74*, 51.
- (51) Schie, M.; Marchewka, A.; Müller, T.; De Souza, R. A.; Waser, R. *J. Phys.: Condens. Matter* **2012**, *24*, 485002.
- (52) Hirel, P.; Marton, P.; Mrovec, M.; Elsässer, C. *Acta Mater.* **2010**, *58*, 6072.
- (53) Hirel, P.; Mrovec, M.; Elsässer, C. *Acta Mater.* **2012**, *60*, 329.
- (54) Uberuaga, B. P.; Choudhury, S.; Bai, X.-M.; Benedek, N. A. *Scr. Mater.* **2012**, *66*, 105.
- (55) Benedek, N. A.; Chua, A. L.-S.; Elsässer, C.; Sutton, A. P.; Finnis, M. W. *Phys. Rev. B* **2008**, *78*, 064110.
- (56) Chua, A. L.-S.; Benedek, N. A.; Chen, L.; Finnis, M. W.; Sutton, A. P. *Nat. Mater.* **2010**, *9*, 418.
- (57) Bishop, S. R.; Marrocchelli, D.; Chatzichristodoulou, C.; Perry, N. H.; Mogensen, M. B.; Tuller, H. L.; Wachsmann, E. D. *Annu. Rev. Mater. Res.* **2013**, *44*, 140228162707002.
- (58) Plimpton, S. J. *Comput. Phys.* **1995**, *117*, 1.
- (59) Hockney, R. W.; Eastwood, J. W. *Computer Simulation Using Particles*; CRC Press: Bristol England; Philadelphia, PA, 1989.
- (60) Burbano, M.; Marrocchelli, D.; Watson, G. W. *J. Electroceram.* **2014**, *32*, 28.
- (61) Burbano, M.; Nadin, S.; Marrocchelli, D.; Salanne, M.; Watson, G. W. *Phys. Chem. Chem. Phys.* **2014**, *16*, 8320.
- (62) Marrocchelli, D.; Madden, P. A.; Norberg, S. T.; Hull, S. *Chem. Mater.* **2011**, *23*, 1365.
- (63) Norberg, S. T.; Hull, S.; Ahmed, I.; Eriksson, S. G.; Marrocchelli, D.; Madden, P. A.; Li, P.; Irvine, J. T. S. *Chem. Mater.* **2011**, *23*, 1356.
- (64) Burbano, M.; Norberg, S. T.; Hull, S.; Eriksson, S. G.; Marrocchelli, D.; Madden, P. A.; Watson, G. W. *Chem. Mater.* **2012**, *24*, 222.
- (65) Jia, C.; Thust, A.; Urban, K. *Phys. Rev. Lett.* **2005**, *95*, 225506.
- (66) Jia, C. L.; Houben, L.; Urban, K. *Philos. Mag. Lett.* **2006**, *86*, 683.
- (67) Ertekin, E.; Srinivasan, V.; Ravichandran, J.; Rossen, P. B.; Siemons, W.; Majumdar, A.; Ramesh, R.; Grossman, J. C. *Phys. Rev. B* **2012**, *85*, 195460.
- (68) Ahn, K.; Chung, Y.-C.; Yoon, K. J.; Son, J.-W.; Kim, B.-K.; Lee, H.-W.; Lee, J.-H. *J. Electroceram.* **2014**, *32*, 72.
- (69) Rupp, J. L. M.; Fabbri, E.; Marrocchelli, D.; Han, J.-W.; Chen, D.; Traversa, E.; Tuller, H. L.; Yildiz, B. *Adv. Funct. Mater.* **2014**, *24*, 1562.
- (70) Zhang, F.; Walker, A. M.; Wright, K.; Gale, J. D. *J. Mater. Chem.* **2010**, *20*, 10445.
- (71) Kuru, Y.; Marrocchelli, D.; Bishop, S. R.; Chen, D.; Yildiz, B.; Tuller, H. L. *J. Electrochem. Soc.* **2012**, *159*, F799.
- (72) Chueh, W. C.; McDaniel, A. H.; Grass, M. E.; Hao, Y.; Jabeen, N.; Liu, Z.; Haile, S. M.; McCarty, K. F.; Bluhm, H.; El Gabaly, F. *Chem. Mater.* **2012**, *24*, 1876.
- (73) Feng, Z. A.; El Gabaly, F.; Ye, X.; Shen, Z.-X.; Chueh, W. C. *Nat. Commun.* **2014**, *5*, 4374.
- (74) De Souza, R. A.; Metlenko, V.; Park, D.; Weirich, T. E. *Phys. Rev. B* **2012**, *85*, 174109.
- (75) Lee, H.-S.; Mizoguchi, T.; Mistui, J.; Yamamoto, T.; Kang, S.-J. L.; Ikuhara, Y. *Phys. Rev. B* **2011**, *83*, 104110.
- (76) De Souza, R. A. *Phys. Chem. Chem. Phys.* **2009**, *11*, 9939.
- (77) De Souza, R. A.; Fleig, J.; Maier, J.; Zhang, Z.; Sigle, W.; Rühle, M. *J. Appl. Phys.* **2005**, *97*, 053502.
- (78) Göbel, M. C.; Gregori, G.; Maier, J. *Phys. Chem. Chem. Phys.* **2014**, *16*, 10214.
- (79) Denk, I.; Münch, W.; Maier, J. *J. Am. Ceram. Soc.* **1995**, *78*, 3265.
- (80) Islam, M. S. *Solid State Ionics* **2002**, *154*, 75.
- (81) Islam, M. S.; Davies, R. A. *J. Mater. Chem.* **2004**, *14*, 86.
- (82) Huang, K.; Tichy, R. S.; Goodenough, J. B. *J. Am. Ceram. Soc.* **1998**, *81*, 2565.
- (83) Stäuble-Pümpin, B.; Ilge, B.; Matijasevic, V. C.; Scholte, P. M. L. O.; Steinfurt, A. J.; Tuinstra, F. *Surf. Sci.* **1996**, *369*, 313.
- (84) De Souza, R. A.; Ramadan, A.; Hörner, S. *Energy Environ. Sci.* **2012**, *5*, 5445.
- (85) Kushima, A.; Yildiz, B. *J. Mater. Chem.* **2010**, *20*, 4809.
- (86) Hinterberg, J.; Zacherle, T.; De Souza, R. A. *Phys. Rev. Lett.* **2013**, *110*, 205901.

- (87) Rushton, M. J. D.; Chroneos, A. *Sci. Rep.* **2014**, *4*, 6068.
- (88) Mayeshiba, T.; Morgan, D. *Phys. Chem. Chem. Phys.* **2014**, *17*, 2715.
- (89) Kilner, J. A. *Solid State Ionics* **2000**, *129*, 13.
- (90) Chen, Y.; Cai, Z.; Kuru, Y.; Ma, W.; Tuller, H. L.; Yildiz, B. *Adv. Energy Mater.* **2013**, *3*, 1221.
- (91) An, J.; Shim, J. H.; Kim, Y.-B.; Park, J. S.; Lee, W.; Gür, T. M.; Prinz, F. B. *MRS Bull.* **2014**, *39*, 798.
- (92) Kuklja, M. M.; Kotomin, E. A.; Merkle, R.; Mastrikov, Y. A.; Maier, J. *Phys. Chem. Chem. Phys.* **2013**, *15*, 5443.